Austrian Marshall Plan Foundation

Final Report

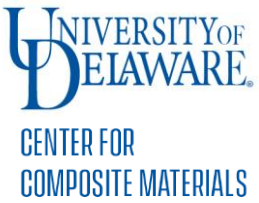

Steerability Evaluation of Tailored Universal Feedstock for Forming Tape Material in the Automated Tape Placement Process and Optimization of the Process with Machine Learning

Alexander Legenstein

Supervisor home university: Prof. Dr. Ralf Schledjewski
Supervisor host university: Dr. Thomas Cender

Leoben, March 31st 2023

This final report documents the outcome of the research stay at the University of Delaware, Center for Composite Materials (UD-CCM). Some results of this report are published in the conference proceedings of SAMPE NA 2023 in Seattle, other results based on this work will be published in the form of journal papers.

This report is not meant for publication, but the corresponding conference and journal papers.

Table of contents

1 Abstract

Tailored universal Feedstock for Forming (TuFF) is a highly aligned discontinuous fiber composite material. A TuFF lamina can be stretched in the fiber direction at processing temperatures due to discontinuous fiber format. This deformation mode allows the production of complex shapes while maintaining high mechanical properties. Steering of continuous fiber materials are limited to a large minimum steering radius to minimize compression wrinkle defects. In-situ stretching of TuFF tape during Laser Assisted-Automated Fiber Placement (LA-AFP) has demonstrated tape steerability over an order of magnitude beyond the current state of the art. This paper develops a methodology to quantify the material strain and placement accuracy for stretch-steered TuFF tape to systematically optimize process variables. A methodology is developed for patterning TuFF tape (3 mm long IM7/PEI, 57% FVF) for reliably measuring the axial and transverse strain after tape placement using photogrammetry. The measurements also quantify the variability in strain components along the tape length. The results are shown to give good agreement with the theoretical prediction used to control the LA-AFP process. It is also shown that by optimally placing the center of rotation of the placement head at the nip-point (where tape is welded to the substrate) the placement accuracy and geometric conformity is two orders of magnitude beyond the current state of the art - 12.5 mm wide tape on a 50 mm radius of curvature - can be achieved without identifiable defects. A machine learning model has been implemented to predict wrinkles during steering. The model utilizes IR images of the tape captured during steering. The binary classification shows an accuracy of 99%.

2 Introduction

In the first section of this report, the theoretical Background to fiber reinforced plastics, automated tape placement and steering is presented. Current limitations in the state of the art of tape steering in terms of minimum steering radius are discussed. Furthermore, methodologies to measure the deformations of tapes during steering are evaluated. After the theoretical foundation, the accuracy of the strain application mechanism is determined and potential influences on the strain development are evaluated. In the next step a methodology to measure the strain and quantify the path deviation of tapes placed at processing conditions is described. With the help of these newly established methodologies, an optimization framework is presented. The path deviation is quantified and minimized, the accuracy of the strain measurement is evaluated and the strain development during steering of 12.5 mm wide tapes at 100 mm steering radius is evaluated. The presented methodologies are then translated to smaller steering radii and with a set of optimal applied strain and tool center point off-set, the minimum steering radius of 12.5 mm wide TuFF/PEI tapes is found.

After the steerability evaluation, data collected from infrared thermography is evaluated to use as input for a machine learning model. The current state of the art in defect detection with infrared methods in AFP and an introduction to convolutional neural networks is presented. The machine learning model established in this work serves as first step for developing a methodology to predict defects during tape steering, especially wrinkles. This report evaluates the feasibility of the collected infrared thermography videos. The videos are split into individual frames and a convolutional neural network is used for a binary prediction of the classes *wrinkle* and *no wrinkle*.

3 Steerability Evaluation

3.1 Theoretical Background

Fiber Reinforced Composites (FRC) consist of two of more physically or chemically different materials, which can be clearly separated. FRCs can be divided into metal matrix composites, ceramic matrix composites, carbon/carbon composites or polymer matrix composites. Polymer matrix composites utilize either thermoset, thermoplastic or elastomers as matrix. [1]

The matrix of FRCs is reinforced by fibers most commonly made from glass or carbon. Especially thermoplastic based composites offer the ability for a better recyclability compared to thermoset composite structures. [1] Furthermore, thermoplastic materials have a higher storage lifespan, which leads to a near infinite shelf life. Thermoset composites need to be refrigerated and last in general 6 months. Especially for large structures, thermoplastic materials offer reduced production time due to the possibility of inline consolidation. [2,3] The reinforcement material of FRCs can be continuous or discontinuous. Continuous fibers allow high mechanical properties, whereas discontinuous fibers allow for greater part complexity. The higher design flexibility enables the use of forming methods, which increase the productivity. Furthermore, different fiber types can be combined to achieve highly tailored material properties. There are currently two hydrodynamic alignment technologies, which can utilize different fiber types and can achieve high levels of alignment with short fibers. There are numerous different aligned discontinuous fiber composites, that have been developed in recent years like. High Performance Discontinuous Fibre method (HiPerDiF), Tailored Universal Feedstock for Forming (TuFF), Stretch Broken Carbon Fiber (SBCF) or DiscoTex. [4,5]. Fiber alignment, aspect ratio, fiber dispersion and fiber matrix adhesion are

essential for achieving optimal mechanical performance of short-fiber reinforced composites [6].

With the steadily increasing demand for fiber reinforced composites the need for automation and reliability has made Automated Fiber Placement (AFP) a process of critical importance. Laser-Assisted Automated Fiber Placement (LA-AFP) process is currently being explored to increase the design scope and address manufacturing challenges by steering fiber tows along curved paths. These Variable Angle Tow (VAT) laminates offer the possibility to reduce weight while enabling a higher flexibility in design to address complex load cases [7,8]. VAT for example have been applied to aircraft wings in order to improve performance. A wing with VAT and with the conventional manufacturing method have been evaluated in this study. For a conventional wing with an aspect ratio of 9, the wing mass can be decreased by up to 32% and the fuel burn reduced by 2.3% by utilizing optimized paths. Moreover, it is possible to manufacture wings with higher aspect ratio with fiber steering. Higher aspect ratios increase the lift of the wing and can therefore reduce the fuel burn. [9]

The primary manufacturing limitation for VAT composites is the Minimum Steering Radius (MSR) - which allows for defect free placement. Although these laminates offer improved properties compared to conventional constant stiffness laminates, defects like gaps, overlaps, misalignment or tow buckling can occur more easily [10]. During the steering of continuous fiber slit tape, the inside radius experiences compressive strains, whereas the outside radius experiences tensile strains, thus resulting in buckling of the inside edge and tow pull-up on the outside edge if the steering radius is too small [11]. Blom [12] reported a MSR of 635 mm for 3.175 mm wide thermoset tapes. Lamontia et al. [13] reported a minimum radius of 1270 mm for 12 simultaneously steered 6.35 mm PEEK tows. Nagendra et al. [14] achieves a

minimum steering radius of 635 mm with 12 simultaneously steered 3.175 mm epoxy tapes. Beakou et al. [15] reported an increase of the MSR from 1500 mm to 4000 mm with an increase of lay-up speed from 12 to 30 m/min for experimental trials and a MSR of 650 mm for 6.35 mm tows from a numerical simulation. Bakhsi and Hojjati [16] placed 6.35 mm wide epoxy tapes at a MSR of 889 mm without defects. Other studies showed a MSR of 800 mm for 6.35 mm wide PEEK tapes [17], 1350 mm for 6.35 mm epoxy tape [18], 1250 mm for 6.35 mm epoxy tape [19] and 800 mm for 6.35 mm PEEK tapes [10]. Smaller steering radii cannot be achieved with continuous tape materials and conventional AFP. Smaller radii have been achieved with Continuous Tow Shearing (CTS). However, CTS produces large changes in thickness and tow width with respect to the shear angle and the maximum shear angle limits the design space. Shear angles of 90° are not possible as this would result in an infinite thickness of the tape. A further limiting factor is the material that can be used in CTS. Conventional prepreg tapes tend to wrinkle due to the high viscosity of the matrix. This constrains the shearing of the fibers [20–22].

Highly aligned discontinuous fiber tape has been demonstrated to close the gap between defect free steering, high mechanical performance, and laminate design flexibility. Due to the discontinuous nature of TuFF, viscous shear load transfer and relative sliding of adjacent fibers [23] allows a prepreg ply to elongate (stretch) in the fiber direction in excess of 40% [24]. By leveraging this fiber direction stretch capability, steering radii an order of magnitude smaller compared to the MSR of continuous 6.35 mm tape can be achieved without any major defects [25].

Figure 1 schematically shows the material deformation objective for stretch-steering TuFF tape along a curvature. Compressive and tensile strains naturally develop when placing wide tape along a curved path due to the geometric difference in path length on the inside and outside tape edges relative to the center line. The strain at

each edge (ε_e) is described in Equation 1, where w is the tape width and R_c is the radius of curvature of the programmed path (at the centerline).

$$\varepsilon_e = \pm \frac{w}{2R_c} \tag{1}$$

In order to prevent compression on the inside tape edge, an in-situ tensile strain is applied (ε_a). When the applied strain is $\varepsilon_a \geq w/(2R_c)$, the inner edge strain will be $\varepsilon_i \geq 0$. Stretch of the outer tape is also required for the tape to conform geometrically. The outer edge strain will be $\varepsilon_o = \varepsilon_a + w/(2R_c)$. The material and processing objective has 3 components which will define a process window: (*i*) prevent the inside edge from wrinkling, (*ii*) limit the strain on the outside edge to avoid tearing, and (*iii*) reliably achieve a linear strain gradient across the tape width so that the overall tape width does not change.

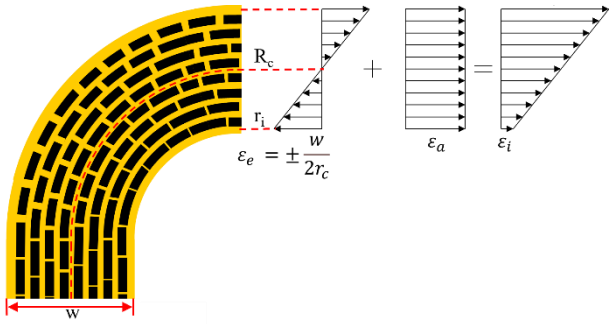

Figure 1. Stretchability of TuFF along curvature and resulting strain gradient across the width due to the offset strain.

Since in-situ stretch-steering of TuFF on highly curved paths relies on achieving the strain gradient described in Figure 1, a novel methodology was developed to measure strain in a thermoplastic slit tape after LA-AFP. Slit tapes were prepared with a regular point pattern which was maintained through the LA-AFP stretch steering process. Photogrammetry was used to measure the local strain tensor along the length and across the width of 12.5 mm (0.5 in) tape. The measurement methodology was then used to evaluate placement accuracy in order to determine

the optimal center of rotation (TCP off-set) at the nip-point - which was determined critical for highly curved paths. The strain measurement methodology was used to evaluate strain variability (due to material variability) and measure the strain gradient from the inside edge to outside edge to confirm the validity of the theory described in Equation 1. With an accurate setting of the TCP and understanding of the required applied strain to avoid inner edge wrinkles, the optimized conditions were applied to evaluate the accuracy at smaller steering radii. Paths with 50 mm radius of curvature provide successful results - two orders of magnitude smaller than achievable for 12.7 mm continuous fiber unidirectional tape. Placement on a 25 mm radius demonstrated minor wrinkling and tape width narrowing, which shows that 25 mm is smaller than the MSR for the current LA-AFP head configuration or requires further process optimization.

3.2 Experimental Methods

3.2.1 Material

This study utilized unidirectional TuFF prepreg which consisted of 3 mm long IM7 fibers and Ultem 1000 thermoplastic Polyetherimide (PEI) matrix, consolidated to 57% fiber volume fraction and 120 gsm fiber areal weight. Each TuFF/PEI prepreg sheet was produced to a width of 559 mm x 432 mm (22 in x 17 in). The fibers were oriented in the 432 mm direction.

Before slitting the prepreg into 432 mm long 12.5 mm wide tapes, the entire prepreg sheet was patterned with points in order to measure the in-plane tape deformation after stretch steering. An equilateral triangular point grid was applied utilizing a vinyl stencil and high temperature spray paint. The point grid consisted of points with 1 mm diameter with a center point spacing of 2.1 mm, which produced 7 rows of points across the 12.5 mm wide tape after slitting. White high temperature spray paint was applied to the prepreg sheet, after which the vinyl stencil was removed. To prevent the spray-painted points from smearing during LA-AFP, the prepreg sheet was reconsolidated to press the paint into the surface. After pressing, the points could not be removed with acetone, which confirmed that the pattern was stable.

The prepreg was slit using a rotary trimmer. The slit tapes were measured to have a width of 12.53 mm with a standard deviation of 0.06 mm. All slit tapes are dried at 120°C for 24 h before being used in LA-AFP. A set of continuous CF/PEI substrates were constructed for this study to avoid substrate related defects.

3.2.2 System and Process Control

All experiments are conducted utilizing a single tow LA-AFP system by Mikrosam. The placement head is equipped with a 3.2 kW laser for heating the substrate laminate and the incoming tape. Consolidation is achieved using a silicone

consolidation roller. The laser power was set to maintain a nip-point temperature of 450±10°C and a re-feed roller velocity of 15 mm/s for all samples. A compaction force of 400 N was used which deformed the silicone roller to a contact length of approximately 20±1 mm.

The method to in-situ stretch the thermoplastic TuFF tape during placement (described by Füssel et al 2022 [25]) employs the consolidation roller to apply a differential velocity relative to the re-feed roller feed rate. When the consolidation roller velocity is higher than the re-feed speed, the tape is subjected to tension loads and stretches to accommodate the defined length change. Figure *2* shows a schematic of the in-situ tape stretching process. Since the process is displacement controlled, Equation 2 describes the in-situ applied strain ε_a as the difference in velocity between the placement head V_2 and the incoming tape feed rate V_1 relative to the incoming tape feed rate. The incoming tape (at room temperature) cannot stretch. As the thermoplastic TuFF tape heats above the glass transition temperature when it passes through the laser heated zone, the polymer softens which allows the tape to stretch. Strain progressively develops in this heat zone until it reaches the nip-point and is welded to the substrate.

$$\varepsilon_a = \frac{V_2 - V_1}{V_1} \tag{2}$$

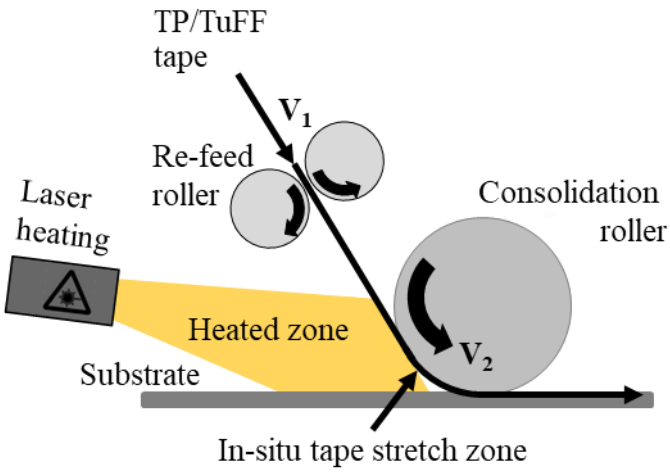

Figure 2. Process control applied in-situ stretching of TuFF tape in LA-AFP

3.2.3 Strain Measurement Method and Digital Image Correlation

Photogrammetry was used to measure the in-plane strain on the stretch-steered tape from the prepared point pattern. The GOM ARGUS system was used to triangulate and assemble the point grid to a mesh in 3D space and compute the strain tensor. Unlike Digital Image Correlation (DIC) [26,27], this technique does not require a reference measurement to an undeformed state since the pattern is predefined. However, references were created for all samples to minimize error in this work. The principle of photogrammetry is shown in Figure 3. A single camera system is used and multiple pictures from the measurement object are taken in different positions around the object. Ray-tracing is used to correlate the points in the individual image to generate a 3D model of the object.

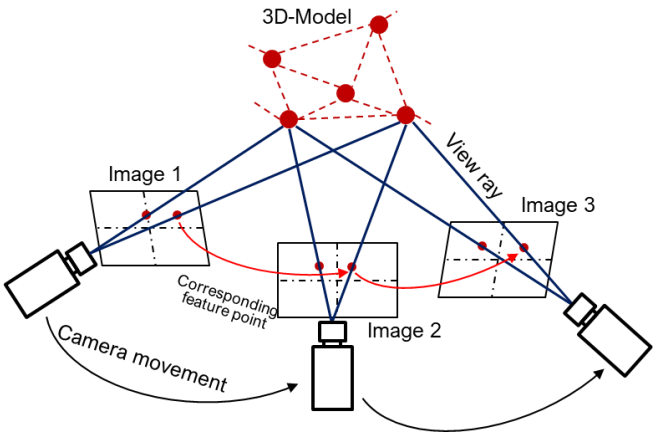

Figure 3: Principles of photogrammetry

The system utilizes a Nikon D500 camera (5569 x 3712 px) with a focal length of 25 mm. The photogrammetry computation is carried out by the forming analysis software in GOM Correlate Pro. To evaluate the errors which arises from assuming the reference patterning is perfect, all slit tapes are analyzed before steering. Without a reference pattern, an error of ~±1.5% strain would propagate into the

post-deformation results. Therefore, in this work, an automated start pattern was used to find the actual initial location of each point as the reference state.

Figure 4a shows an example of a patterned tape before and after placement. The tape on top shows the patterned surface before deformation and below is the same tape after placement with 40% strain applied in longitudinal direction. Figure 4b shows an example of how the point grid is triangulated before and after deformation.

Digital image correlation is used for evaluating the velocities of the re-feed roller and the placement head. Reference markers are used on the measurement objects. The DIC system uses two cameras to track the markers in 3D space. The cameras used for the tracking have a 12 MP resolution and can record with up to 150 frames/s. The lenses have a focal length of 12 mm. Multiple light sources are used to ensure illumination while keeping the exposure time low.

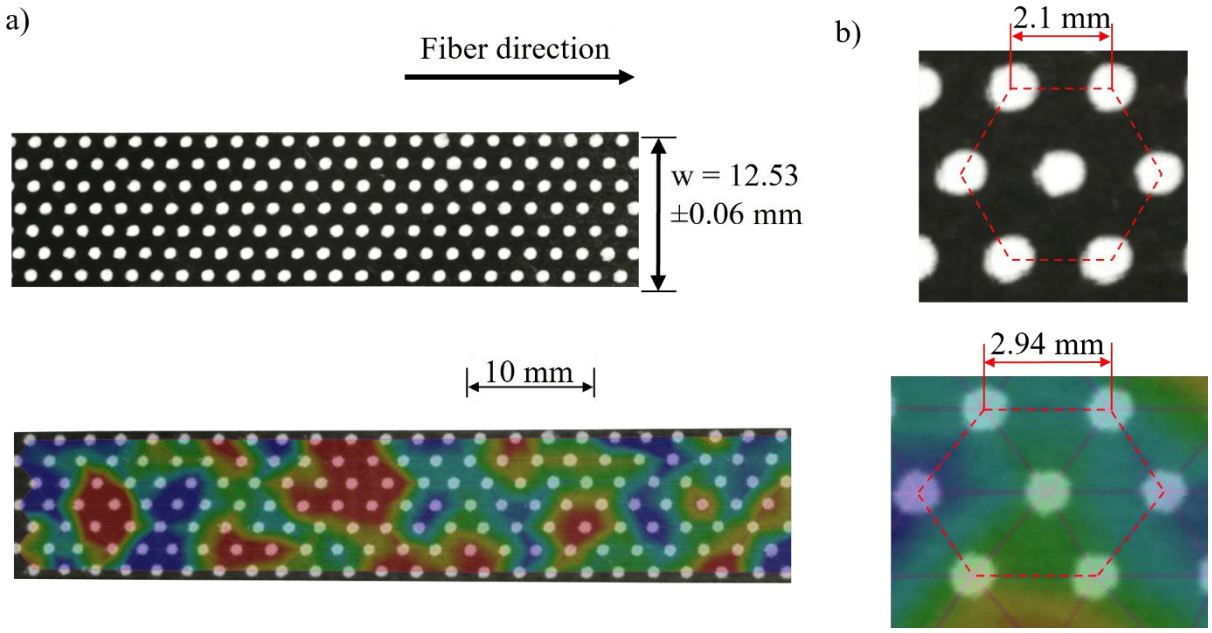

Figure 4. a.) Point grid on TuFF/PEI tape with strain map. b.) Mesh before and after steering at $\boldsymbol{\varepsilon_a} = 40\%$

3.3 Steerability Evaluation

To optimize the process settings for stretch-steering of thermoplastic TuFF tape on highly curved paths, the methodology follows 5 sequential steps.

1. Evaluate the accuracy of strain application mechanism
2. Measure the strain on tape placed along straight paths
3. Locate the tool center point (TCP) at the nip-point
4. Measure the strain across the tape width after stretch-steering on a curved path
5. Evaluate the optimized process conditions to determine the minimum steering radius

The first step is used to evaluate the accuracy of the re-feed roller and the placement head movement in terms of velocities. This assessment is used to determine the error due to the placement equipment. Any variability in the can lead to a difference in applied strain (see Equation 2). The second step is used to determine the accuracy of an applied strain ε_a. This quality evaluation determines the material variability and the strain limit that can be achieved (on an outer path edge) during the steering experiments. The third step is critical for highly curved paths. By default, the center of rotation (at the TCP) is at the center of the roller consolidation area which is behind the nip-point. For small radius paths, the center of rotation must be placed at the nip-point for the tape to follow the programmed path. The fourth step is to determine how strain across the width of the tape correlates to the description in Figure 1. By assessing the strain variability in step 1 and the strain on the inside edge in step 3, an appropriate applied strain can be set according to the tape width and path curvature which will ensure the inside tape edge does not wrinkle. The

fifth step is a validation to ensure that the nip-point location and applied strain can accurately place the tape on the programmed path and avoid wrinkles.

3.3.1 Movement analysis of tape placement head

In order to determine the accuracy of the strain application mechanism, a straight path with 10% applied strain is placed without any tape material or heat input. To

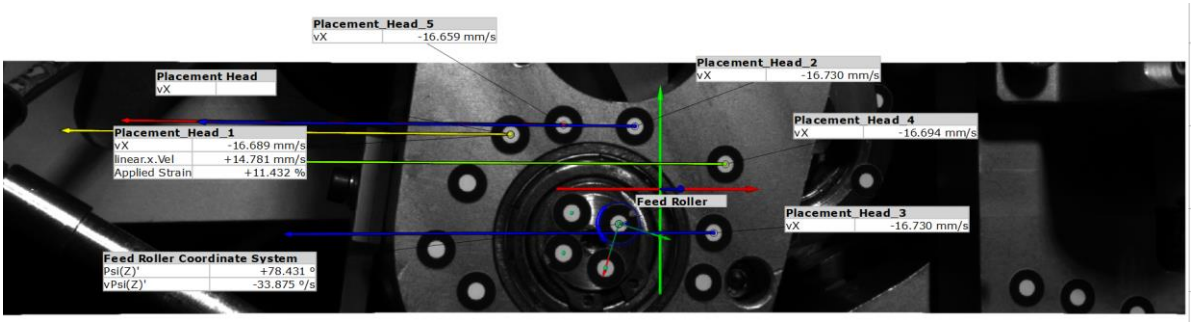

Figure 5: Re-feed roller and parts of the placement head with reference markers. The movement of the head is annotated with vectors.

measure the movement of the re-feed roller and the placement head, a number of 3 mm reference markers are placed on the drive of the re-feed roller and on the placement head. The configuration can be seen in Figure 5. A DIC system is used to track the reference markers and calculate the velocities. The linear velocity is measured on 4 points. The rotational velocity of the re-feed roller is measured with three points, which are connected by a coordinate system. Both the linear as well as the rotational velocity are measured relative to a fixed coordinate system in the measurement space. The rotational velocity is transformed into a linear velocity by multiplying it with the radius of the re-feed roller (25 mm). The data of the DIC for the linear velocity of the re-feed roller is compared to the data measured by the Programmable Logic Controller (PLC). The PLC has a measurement frequency of 500 Hz, whereas the DIC measures at a frequency of 150 Hz. A Fast Fourier Transform (FFT) is used to identify any discrepancies between the PLC and the DIC data. The results of the FFT can be seen in Figure 6.

The data from the PLC and DIC for the linear velocity of the re-feed roller show the same dominant peak at the 17.2 Hz. This validates the measurement technique as it aligns with the data from the PLC. The linear velocity of the placement head

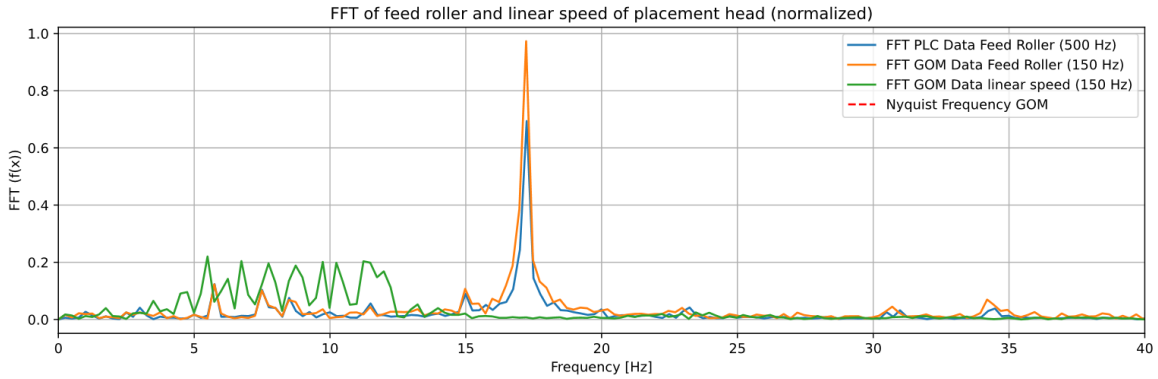

Figure 6: FFT of the re-feed roller and the placement head linear velocities

shows no dominant frequency. The effects of these frequencies manifest itself in a variability of the applied strain. Figure 7 shows the influence of the variability of the re-feed roller and placement head linear velocity of the applied strain. The mean applied strain is 11.37% with a standard deviation of 14.16%. This would result in compression and over stretching at the peaks. The period of the strain oscillation is around 0.5 s. The distance travelled by the tape during the period is smaller compared to the gauge length of the photogrammetry measurement. Therefore, no influence of the strain oscillation is to be expected in the strain measurement. A second set of measurements was conducted with an applied strain value of 80%. The results show a similar trend compared to those at 10%. The mean applied measured strain is higher, than desired applied strain with a standard deviation resulting in strain values of over 100% applied strain at the peaks.

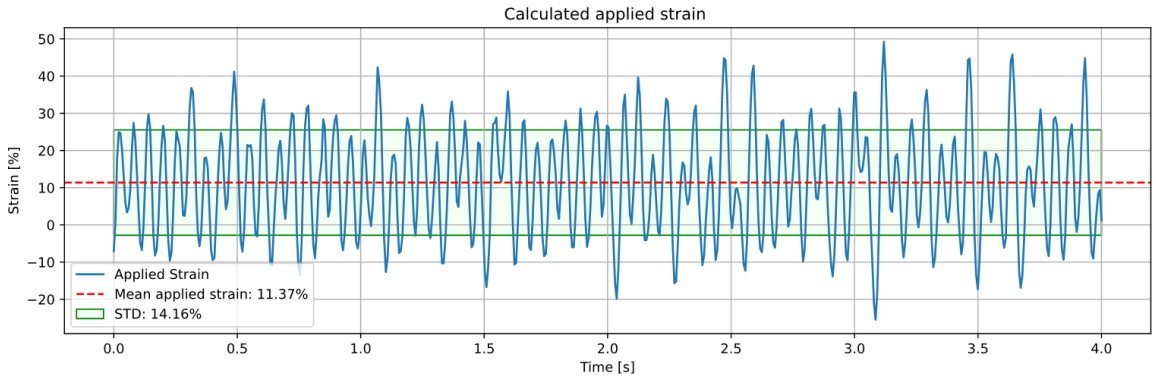

Figure 7: Measured linear velocity of the re-feed roller and placement head are used to calculate the applied strain with Equation 3

3.3.2 In-situ stretching on straight paths

To establish a baseline for the accuracy and repeatability of applied strain a series of straight paths are placed with imposed tensile strains of 3, 5, 10, 20, 40, 60, and 80%. The samples at 5, 10 and 40% are each repeated twice. Figure 8 shows the measured longitudinal strain relative to the applied strain. The stretching can be visually observed in the deformed pattern on the right. The strain measurement region of ~80 mm long section (steady state region in terms of tape velocity and temperature) is used to evaluate the average and standard deviation along the length. Distortion of the pattern for a sample stretched to 80% exceeded the capabilities of the software for correlating the surface components and the strains could not be evaluated. However, visual inspection showed the 80% stretch was feasible.

The graph in Figure 8 shows, that the measured strain in the straight paths fits the applied strain on average but the local variability increases with applied strain. A linear fit to the measured data results in a fitting equation for the measured strain of $\varepsilon = 0.996\varepsilon_a - 0.304$ with a coefficient of determination (R^2) of 0.999. The average axial strain values for repeated samples with 5, 10 and 40% exhibited a standard deviation of 0.16, 0.15 and 0.15% respectively. This demonstrates that the results, including local strain variability, are highly reproducible.

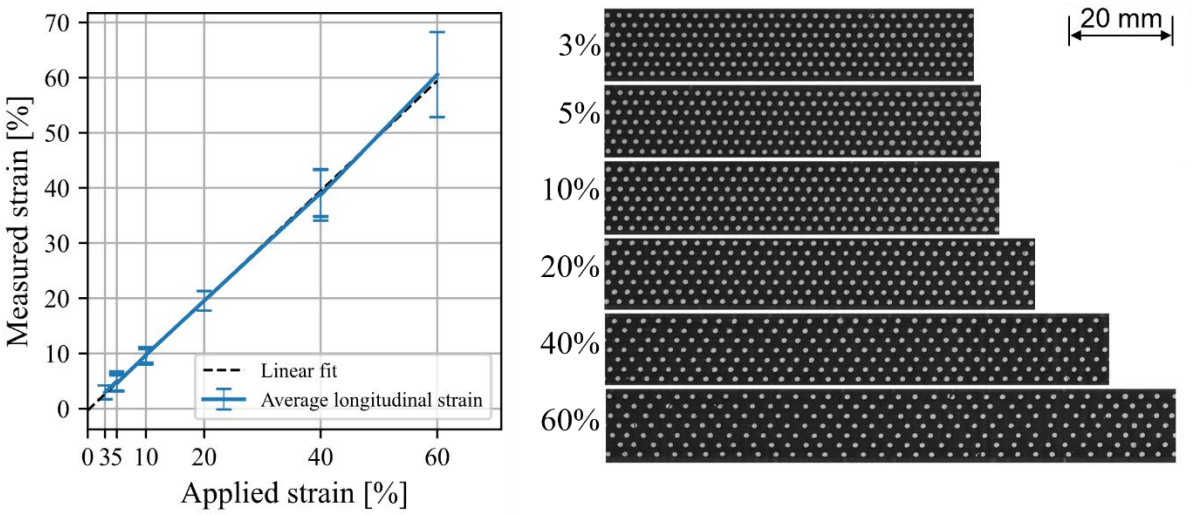

Figure 8. Strain measurement of straight paths with different imposed strain values and a linear fit to the data ($R^2 = 0.999$) (left), deformation of point patterning due to strain (right)

3.3.3 Path Deviation due to TCP off-set

Path deviations can be observed during steering, which become more prominent at small steering radii. The deviation is a function of the programmed radius (R_c) and the position of the center of rotation relative to the nip-point (x_{nip}) of the consolidation roller. A geometric definition for the path deviation is shown in Equation 3. This equation is derived from the geometry of the consolidation roller, the tape width, and the desired radius. The path deviation increases with a decrease in steering radius or an increase in contact length. Figure 9a displays the default TCP position at the center of rotation. The path deviation (ΔP) is the result of the deviation from the actual path to the programmed path, due to the off-set of the center of rotation from the nip-point. With an off-set of the center of rotation to the nip-point, the programmed path follows the actual path (Figure 9b).

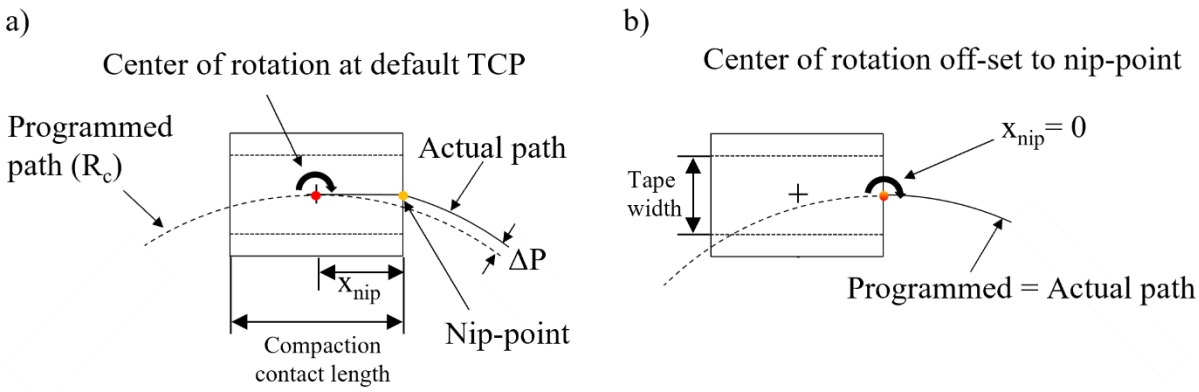

Figure 9. (a) By default, the tool center point (TCP) which is centered under the consolidation roller will not accurately place tapes on curved paths because the tape is welded to the substrate at the nip-point. (b) Off-setting the TCP so that the nip-point follows the programmed path is critical for placement accuracy on highly curved paths.

$$\Delta P = -\sqrt{R_c^2 - x_{nip}^2} + R_c \tag{3}$$

By default, the center of rotation - i.e., the tool center point (TCP) - is centered under the consolidation roller, and thus $x_{nip} = L_c/2$ where L_c is the contact length of the consolidation roller. As described in Equation 3, since the tape is welded to the substrate at the nip-point, the nip-point location must follow the programmed path to achieve accurate placement. The contact length is an unknown and will change as the consolidation force deforms the roller.

Since the exact nip-point location is unknown, a series of tests are required to set a correct TCP. The required TCP off-set is determined by measuring the influence of a changing TCP position on the path deviation. Tapes are placed with a 100 mm steering radius and an applied strain of 10%. All TCP positions are offset towards the direction of the nip-point. TCP off-set values of 0, 6, 7, 8, 10, 14, and 20 mm

were tested to measure the relative placement accuracy. Figure 10a shows the results of the steering experiments.

The path deviation in Figure 10b is quantified based on the difference in the distance measured on the placed paths relative to the programmed path. The centerline position of the placed tapes was measured from the point grid with the photogrammetry analysis. The path deviation is calculated by subtracting the distances from the center point row to the theoretical center point of the radius. Figure 10a shows the programmed paths with a red line and the measured tape centerline with a yellow line.

Figure 10b shows the measured path deviation over the length of each tape. The default TCP (0 mm off-set) results in clearly visible oversteering in Figure 10a, which shown in Figure 10b is 2.5 mm from the programmed path. As the offset is increased toward 10 mm, placement accuracy improved. Offsets of 14 and 20 mm put the center of rotation in front on the nip-point which resulted in understeering in the curved section.

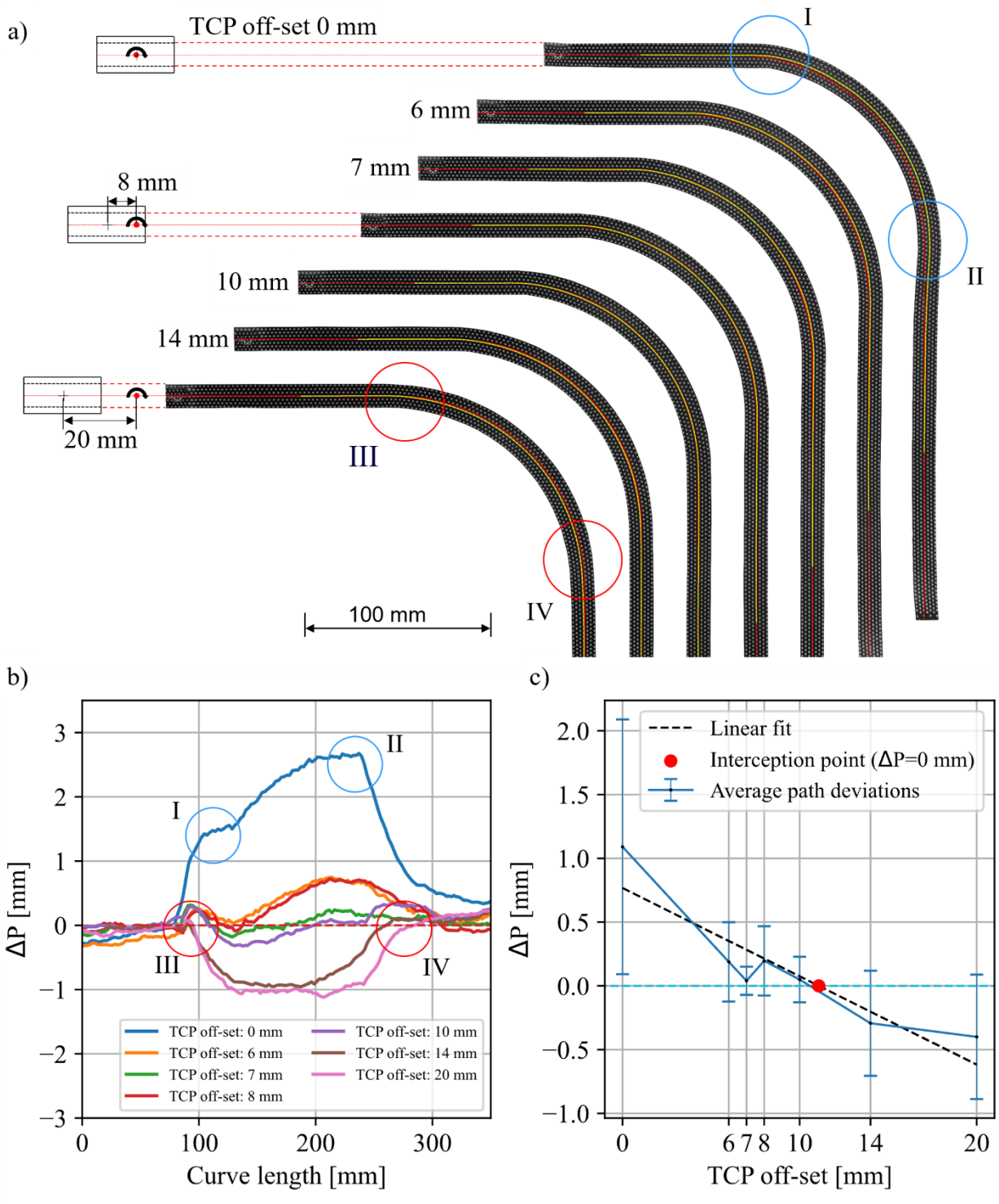

Figure 10. (a) Tapes placed with varying TCP off-set positions. (b) Path deviation over the whole placement length. (c) Calculation of the optimal TCP off-set based on the intersection of a linear fit with $\Delta P = 0$ mm.

3.3.4 Strain gradient across the width during steering

Based on the results of section 3.3.3, a TCP off-set of 11 mm is chosen for evaluating the strain development on steered paths. Tapes were placed with an applied strain of 3, 5, 10, 30 and 40% on 100 mm radius path. Based on the calculations with Equation 1, an applied tensile strain below 6.35% will result in wrinkling of the inside edge of the 12.5 mm wide tape.

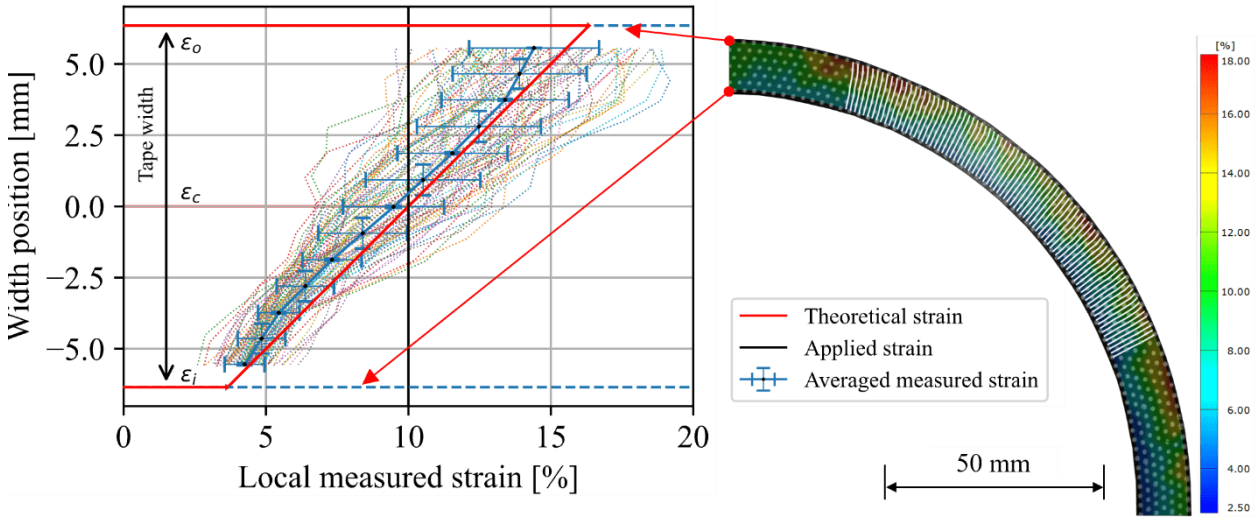

Figure 11. Strain gradient across the width with $\boldsymbol{\varepsilon_a}$ = 10% (left). Steered section with transverse lines in the steady-state steering section (right)

Figure 11 shows the strain development in longitudinal direction across the tape width when 10% strain is applied. Strain is computed in the series of sections across the width (indicated in white) to observe the strain gradient from the inner edge to the outer edge and the variability. The strain on the inside edge (ε_i), the center line (ε_c) and the outer edge (ε_o) strains are annotated in the plot. The strain gradient closely follows the predicted strain across the width shown in Equation 4. The variability in the strain is shown in Figure 11 and is used to describe the necessary applied strain to avoid compression wrinkles.

$$\varepsilon(y) = \varepsilon_a + \frac{y}{2R_c}, \qquad -w/2 \le y \le w/2 \tag{4}$$

Figure 12 shows the results for the effect of varying the applied strain on the steered path. The average strain along the inside, centerline, and outside path is measured for each level of applied strain. As described in Equation 4 the onset of compression wrinkles is expected when the applied strain is below 6.35%. Wrinkling clearly can be observed at applied strain values of 3% and 5%. This result confirms the hypothesis shown in Figure 1. No wrinkling or tearing defects in the steered section of the tapes with 10, 30, and 40% applied strain can be observed. The strain variability shown in the graph in Figure 12 suggests an additional applied strain (safety factor) is required to reliably ensure compression wrinkles do not form. For this radius, an applied strain of approximately 9.35% would be required for wrinkle-free tape steering.

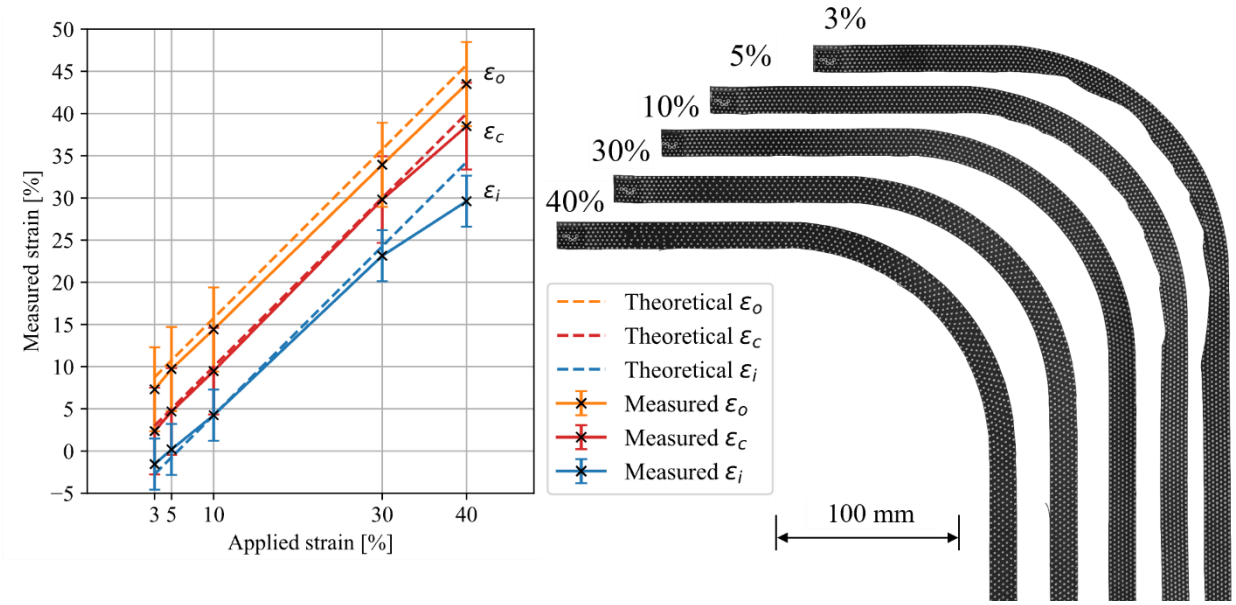

Figure 12. Longitudinal strain along the inner edge $\boldsymbol{\varepsilon_i}$, outer edge $\boldsymbol{\varepsilon_o}$, and centerline $\boldsymbol{\varepsilon_c}$ for tape placed with applied strain $\boldsymbol{\varepsilon_a} = 3$, 5, 10, 30, and 40% on a 100 mm radius.

3.3.5 Minimum Steering Radius

To translate the results found in the previous sections for the process optimization of TuFF steering, tapes were stretch-steered on a 50 mm and 25 mm radius. The

optimal applied strain was chosen based on the strain gradient predicted in Equation 4 and the variability results observed in Figure 12 to include a safety

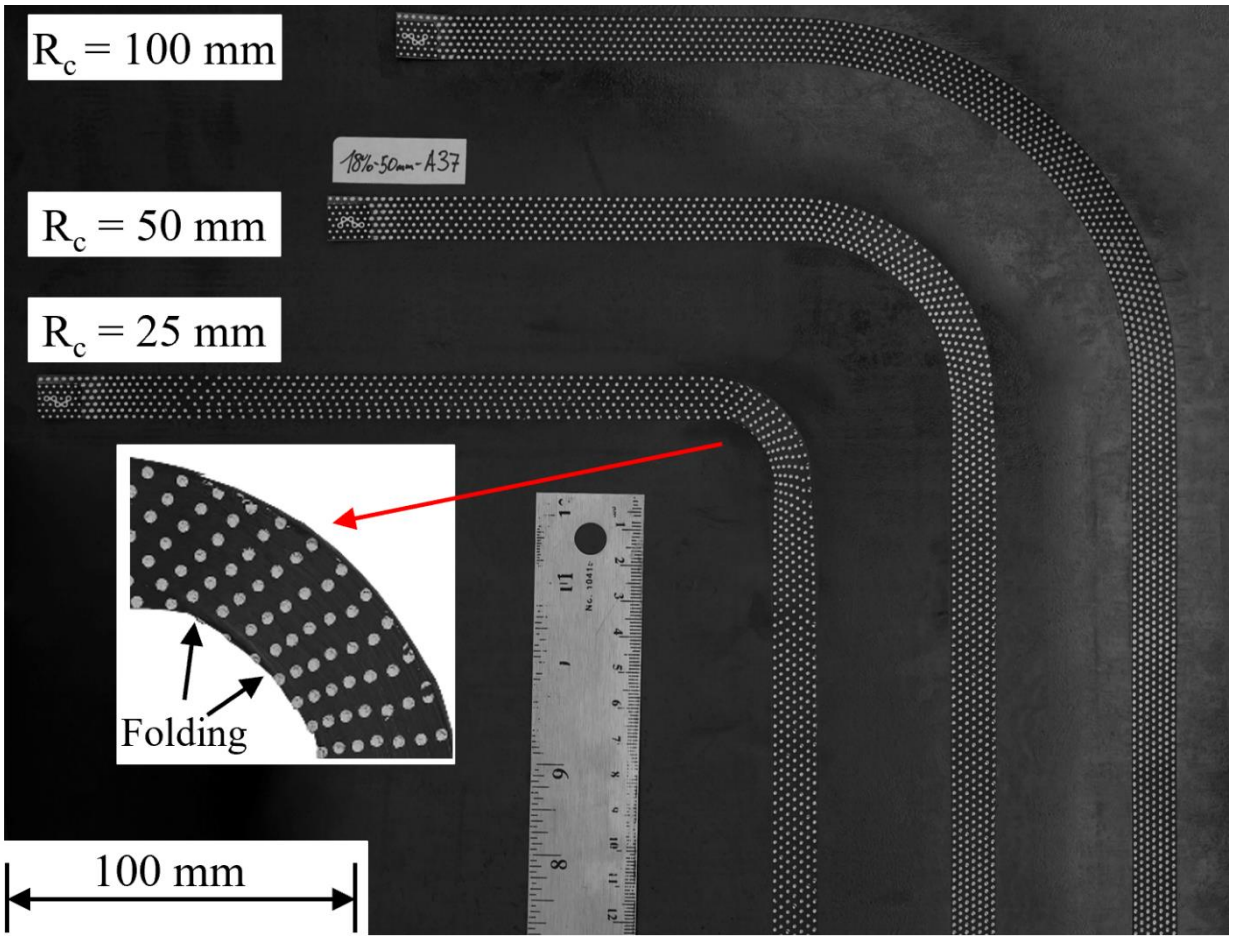

factor. The applied strains were set to 18% for the 50 mm radius and 32% for the 25 mm radius. Figure 13 shows the tape placed on the 50 mm radius with no defects. On the 25 mm steering radius, slight folding of the inside edge is observed as well as slight fraying on the outside edge. Additionally, the width of the tape placed on the 25 mm radius showed significant narrowing. The optimization of the TCP offset to the nip-point (in section 3.3.3) is demonstrated to produce accurate placement results, which according to Equation 3 would otherwise produce a large deviation on a 25 mm radius. With the current head configuration and process parameters, the minimum steering radius of 50 mm for 12.5 mm (0.5 in.) wide tape is demonstrated. Further improvement in the minimum steering radius will quickly approach the strain limit of the material, described in section 3.3.2.

Figure 13. Steering of a 100 mm, 50 mm, and 25 mm radius with $\boldsymbol{\varepsilon_a}$ = 10%, 18% and 32% respectively

Figure 14 puts the results of this study in perspective with other studies, mentioned in section 3.1. TuFF is able to achieve steering radii two order of magnitude smaller compared to the literature. It has to be noted, that the values from Sloan [28] are theoretical values from the manufactures of the listed AFP machines and those values are not backed by experimental data found in the literature. A steering radius of 25 mm could also potentially be counted as MSR if the folding on the inside of the tape is acceptable. Currently, there are no set definition which steering defects would be acceptable. A conservative approach would be, that no defects should be present. Even with this definition, TuFF showes far smaller MSR compared to continuous tape.

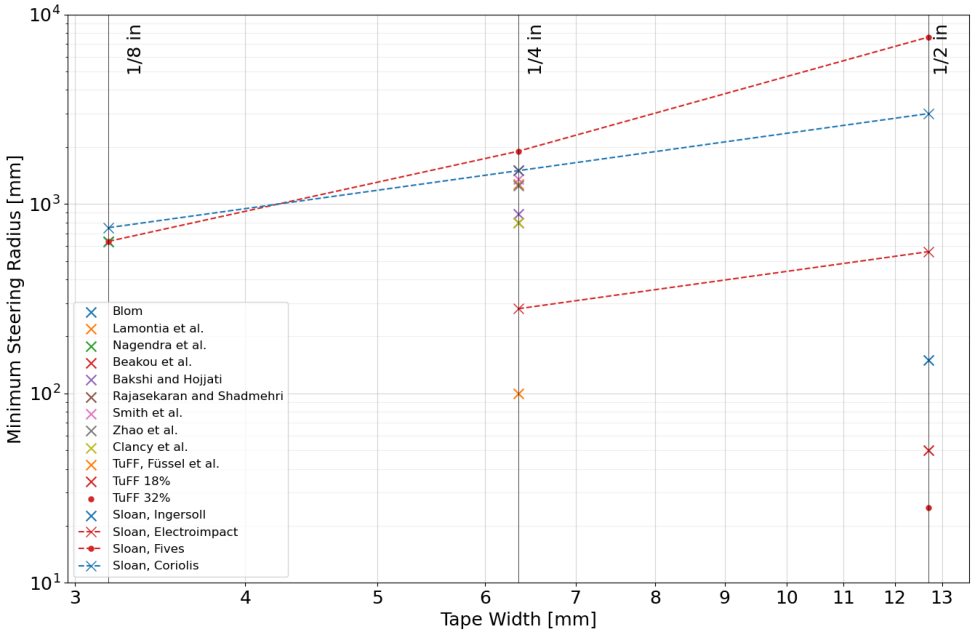

Figure 14: MSR of TuFF compared to continuous tape material [12–15,17–19,10,25,28]

3.4 Conclusions

A methodology for process optimization of stretch-steering thermoplastic matrix aligned discontinuous fiber tapes (TuFF/PEI) was developed and demonstrated.

The material evaluation utilized a novel methodology for measuring the in-plane strain of patterned tapes using photogrammetry. A robust method for preparation of patterned thermoplastic tapes was developed to ensure the pattern was not lost during laser tape placement with in-situ stretching.

Using the measurement methodology, the effect of process parameters on stretch-steered placement quality was determined with a high level of precision. Material strain variability was defined for tapes which were stretched on straight paths and steered paths to determine a safe margin for the maximum applied strain and the onset of wrinkling on the inner edge of a steered path.

A framework was defined for describing the deviation of a placed path due to the distance of the center of rotation from the compaction roller nip-point. The nip-point location was defined based directly on the accuracy of placed paths.

The measurement methodology and process optimization were combined to demonstrate that an optimized process is able to stretch-steer 12.5 mm (0.5 in) wide thermoplastic TuFF tape on a 50 mm radius without defects, which represents a two order of magnitude improvement over what is achievable for 12.7 mm wide continuous fiber tape.

4 Wrinkle Prediction

4.1 Theoretical Background

As discussed in section 3.1, AFP has a high potential to reduce process time and safe cost, due to the high degree of automation. Most of the parts although are still quality checked manually with visual inspection. This increases the processing time and can cause and increase of production time by up to 63%. [29] Not all defects can be detected visually and undetected errors can create catastrophic failure [30]. The most common defects are gaps, overlaps, missing tows, twisted tows, bridging, air pockets, foreign object defects or splices [31]. Croft et al. [32] showed that different mechanical parameters like in-plane shear, open-hole compression and tension strength can be reduced up to 12% due to gaps, overlaps or half gaps and overlaps. Although a sequence of gaps and overlaps seemed to be the most crucial factor. Woigk et al. [33] confirmed the findings of Croft et al. [32], that simultaneously occurring gaps and overlaps reduced the compression strength up to 14.7 % compared to the pristine samples. The tension strength was reduced up to 7.4 %. During steering, defects like tow pull up, wrinkling, tearing or misalignment are most common [34]. There is already some research effort to utilize Infrared (IR) cameras to monitor the tape during lay-up. Denkena et al. [29] used a IR-camera to monitor the lay-up during AFP to analyze temperature differences between the currently placed tow and the surface underneath to detect defects. Yadav et al. [30] also utilizes an IR camera to monitor the tape after the consolidation roller. The temperature gradients are used to detect any surface defects and their exact position. Those defect detection methods currently lack a fast predictability to use them inline and adapt to different defects. Machine Learning (ML) offers the possibility to extract features or make the prediction more independent of the process. This could leverage the current models to be capable of fast reliable inline prediction [35].

ML is a subsection of artificial intelligence. It was defined by Arthur Samuel [36] in 1959 as "[A] Field of study that gives computers the ability to learn without being explicitly programmed". ML unfolds its full potential, when there are complex tasks which cannot be easily solved with traditional programming like speech recognition. It can give insight in data which at first glance is not connected among themselves. ML has already been utilized with the ATP process. Sacco et al. [37] used ML for inspection of the tapes during the process to allow a fast defect detection. Wanigasekara et al. [38,39] used ML to predict the interlaminar shear strength, the elastic modulus, the maximum flexural stress and the maximum strain based on lay up speed, hot gas torch temperature and consolidation force. Furthermore, an inverse ML model was developed to predict the input parameters for the ATP process to achieve desired characteristics of the laminates. Due to the lack of real samples Wanigasekara et al. [38,39] used Virtual Sample Generation (VSG) as a method to enhance the training data set. These techniques are commonly used, due to the time-consuming process of gaining enough data points for machine learning models. Marani et al. [40] uses unsupervised learning to detect subsurface detects utilizing thermography. Schmidt et al. [35] used a Convolutional Neural Network (CNN) to predict early stage material defects in prepregs for the AFP process based on thermal images.

Currently there are no models that have been trained to predict defects arising in tape steering with IR thermography. This work aims to evaluate the feasibility of the data generated by the IR camara during lay-up for classification of wrinkles during steering with a CNN.

Convolutional neural networks are similar to Artificial Neural Networks (ANN). Both are composed of neurons, which optimize themselves through adjusting weights. The difference between both networks is their field of application. CNNs are mainly used for image-focused tasks, due to their ability to work with high dimensionality data, while maintaining a lower complexity compared to ANNs. Most CNNs consist of three main layer types; convolutional, pooling and fully connected layers. Convolutional layers are filters, that allow the network to extract

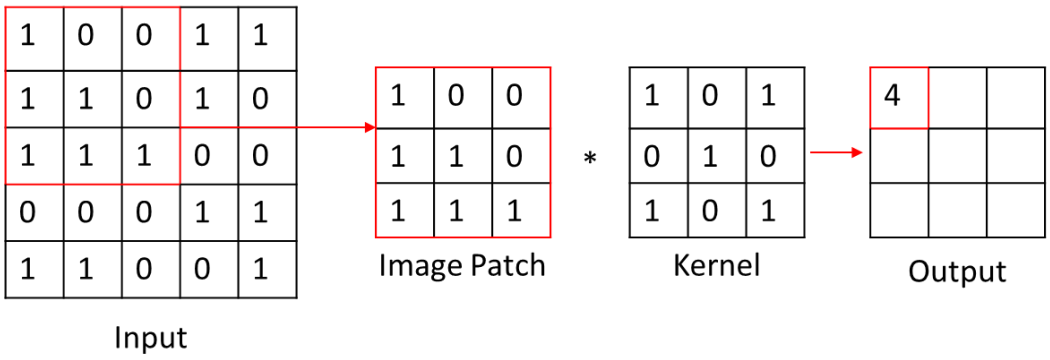

Figure 15: Representation of a convolutional operation

features from the input and create a feature map.

Figure 15 shows a convolutional operation. A patch from the input is selected and multiplied with the kernel and the sum of all multiplications is the output. The pooling layer is used for down sampling the given input and therefore reducing the computational burden. Figure 16 shows a max pooling operation with a 2x2 kernel and a stride of 2 along the spatial dimensions of the input resulting in a size

reduction to 25% of the input map. The fully connected layers are used to for generating the output of the CNN. [41–44]

Activation functions:

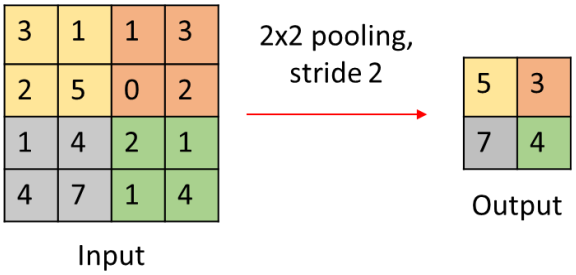

Figure 16: Max pooling operation

After each convolutional layer, activation functions are used to introduce non-linearity, which adjusts the generated output and enables the network to solve complex problems. The most common activation function is the Rectified Linear Unit (ReLU), as it can prevent the vanishing gradient problem associated with other activation functions (e.g. tanh or sigmoid). The ReLU function is defined in equation 5.

$$f(x) = \max(0, x) \tag{5}$$

Besides the ReLU activation function, there are several others, like the sigmoid or tanh functions. The sigmoid function is most commonly used in binary classification in the output layer as it results in an output between 0 and 1, which can be interpreted as probability. The sigmoid activation function is shown in equation 6. [43,42]

$$f(x) = \frac{1}{1 + e^{-x}} \tag{6}$$

Regularization:

Regularization is used to avoid overfitting. A penalty is added to the neural network to make the model generalize better to new and unseen data. If a model

is overfitting it learns the training data noise and the patterns in those datapoints. The result is a model, which performs poorly on new data. The most

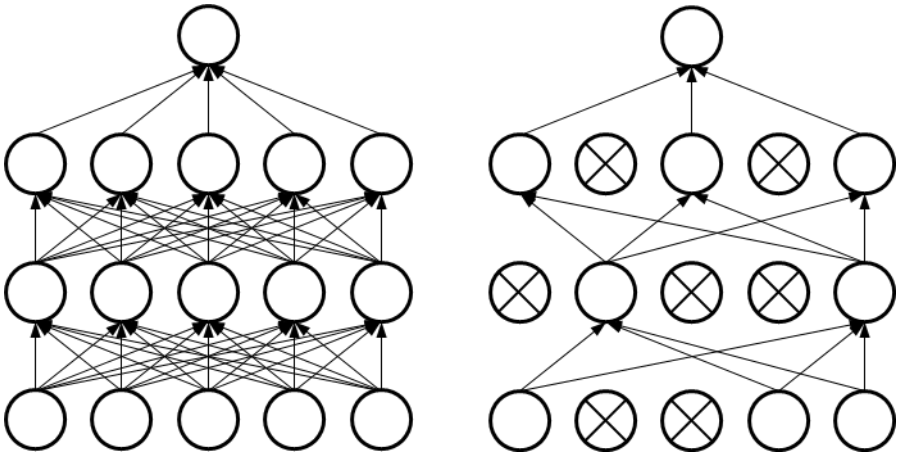

Figure 17: Regular neural network (left), neural network with applied dropout regularization (right)

common regularization methods are L1 and L2 regularization. Dropout regularization randomly drops out (i.e., sets to zero) some of the neurons in the neural network during training (see Figure 17). This helps to make the model less sensitive to the individual weights of the neurons, as neurons have to take over the representation of the dropped out neurons and thus resulting in multiple internal representations. [45]

4.2 Experimental Method

The data for the model is generated by placing two tapes at a 100 mm steering radius at applied strain values of 3% and 5% to ensure wrinkling. The tapes are shown in Figure 12. The data acquisition is started before the laser turns on to capture empty frames and the start-up of the placement. The data acquisition is done with an IR camera from Tachyon. The integration time is set to 200 µs and the frame rate is set to 1000 frames/s. Every fifth frame is saved and used for the evaluation and. The lay-up speed is set to 15 mm/s. The lens has a focal length of 35 mm. The camera can capture images with a size of 128 x 128 pixels. The minimum temperature of detection is 200°C. After the IR videos are collected, they

are post-processed to extract the individual frames. The frames are normalized in a first step to a value range of 0-255 and then divided by 255 to set them to a range between 0 and 1. The input pictures are shown in Figure 18. The left picture shows the tape at the start-up phase, the laser has not reached its processing temperature yet. The middle picture shows the tape in the steady-state region before steering. A temperature gradient from the top to the bottom can be seen. The mirroring underneath the tape is the reflection of tape on the substrate surface. The right picture shows the tape in the steady-state steering section. The wrinkle can be seen on the right edge of the tape. Wrinkling is clearly visible due to the tape lifting off the roller surface and losing the conductive heat transfer to the roller. This prevents the heat from dissipating and increases the local temperature in the tape. All wrinkles used for this study have the same temperature characteristics. All steering is performed in the same orientation and therefore all wrinkles appear on the right side of the tape.

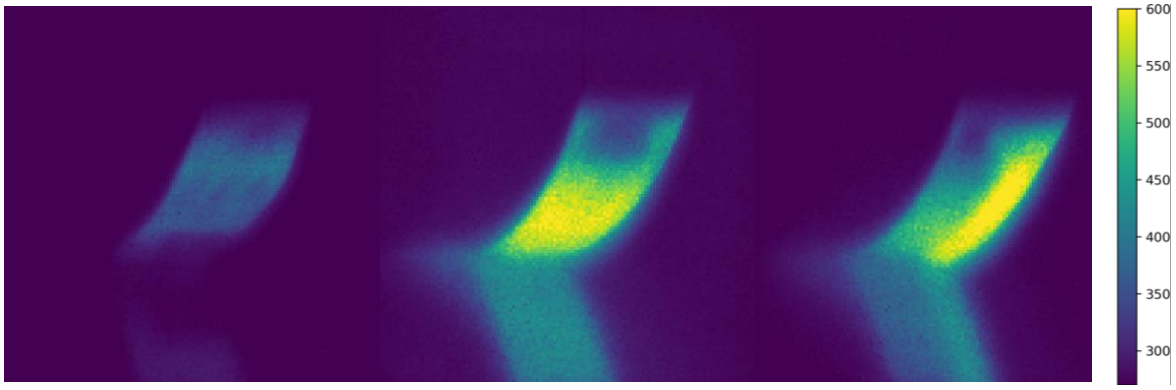

Figure 18: Tape during start up (left), tape during steady state straight line (middle), tape during steady state steering with wrinkle (right)

The dataset consists of 1470 frames. Each frame is labelled as *Wrinkle* or *No Wrinkle*. The thermal images are compared with videos from a camera mounted next to the consolidation roller and the placed tapes to avoid mislabeling. The training data consists of 1032 frames without wrinkles and 438 frames with wrinkles. The dataset is split by utilizing K fold cross validation with 4 folds. This method

helps to evaluate the model with limited amount of data. Additionally to the training data, a tape is placed at a 25 mm radius with 10% applied strain to ensure wrinkling. This data is used in order to calculate precision and recall on the trained model. This dataset consists of 191 frames with no wrinkles and 102 frames with wrinkles. The frames for this evaluation dataset are preprocessed the same as the training samples.

The model for the classification task is a CNN. The network consists of 3 convolutional and max pooling layers. The convolutional kernels are set to a size of 3x3. The max pooling layers use a 2x2 kernel. Dropout regularization is used to avoid overfitting. A rectified linear unit is used as activation function for all layers except the output layer. The output layer uses a sigmoid activation function to yield a probability value. The architecture of the model is shown in Table 1. Early stopping is implemented to limit the training time if the accuracy is not increasing within 3 training epochs. The model is trained for 10 epochs with a batch size of 42 and the Adam optimizer. Different models are trained to find the best model parameters and minimize the classification error.

Table 1: Configuration of the CNN

Layer	**Characteristics**
1	Input of thermal image (512,512,3) and convolution 3-16
2	Max pooling
3	Convolution 3-32
4	Max pooling
5	Convolution 3-128
6	Max pooling
7	Flattening layer
8	Dropout regularization
9	Fully connected layer 128 neurons
10	Classification

4.3 Results

The precision and the recall of the best model are shown in Figure 19. The data for the validation of the model was taken from the steered of a tape steered at 25 mm with 10% applied strain to generate wrinkling and sections before and after the steering. No data from other defects has been used for this evaluation. The model did not predict any false positive values and therefore resulting in a precision of 100%. The recall yields a value of 97.1% due to the misclassification of 3 wrinkles as no wrinkle. The overall capabilities of the model to predict wrinkles is high with an accuracy of 99%.

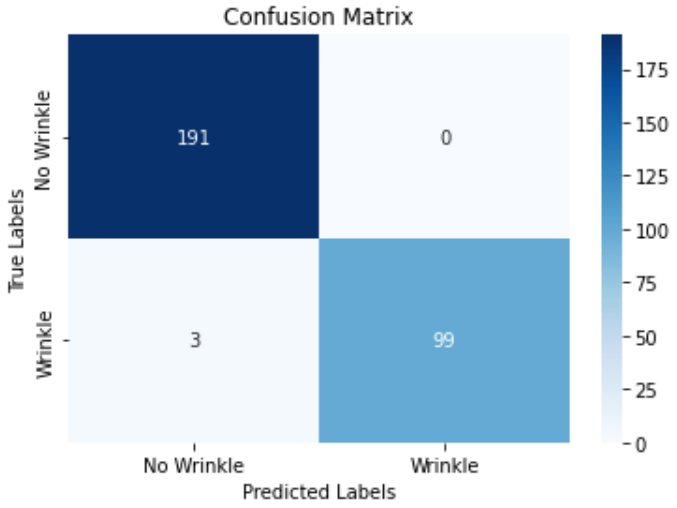

Figure 19: Confusion matrix for classification of wrinkles

4.4 Conclusions

A machine learning model has been trained for binary classification of wrinkles during steering of highly aligned discontinuous fiber materials. The model showed high precision and recall values, which indicates that machine learning is a promising technique to leverage IR thermography to inline process evaluation. The current model is capable of classifying wrinkling or non-wrinkling during the process. The model can be improved by collecting more data and for different defects. Furthermore, detection of the defect positions should be implemented to be

able to exactly locate the defect in the laminate. Semantic image segmentation can be used to categorize each pixel for each defect class. This enables an exact quantification of the defect size. This can help to decide if certain defects are acceptable in the laminate. Furthermore, an in-line detection of defects can be used to decide on early stopping of the process to save processing time and therefore cost.

5 Acknowledgment

I want to thank the Austrian Marshall Plan Foundation, for making this research possible through their scholarship. My deepest gratitude goes to the Center for Composite Materials for offering me this great opportunity and helping me in every aspect during my stay. My special thank goes to Thomas Cender, Dirk Heider, John Gillespie Jr., John Tierney and Lukas Füssel for all the help with my research and for the support in transforming this research into publications. I also want to thank the Montanuniversität Leoben and Ralf Schledjewski for the financial support and the ongoing mentoring and support.

Lastly I also want to thank everyone at the CCM and the University of Delaware, that helped me during my research stay.

6 References

7 References

[1] Erden S, Ho K. Fiber reinforced composites. In: Seydibeyoglu MÖ, Mohanty AK, Misra M, editors. Fiber Technology for Fiber-Reinforced Composites: Deans, Matthew; 2017, p. 51–81.

[2] Denkena B, Schmidt C, Kaczemirzk M, Schwinn M. Influence of a Dynamic Consolidation Force on In Situ Consolidation Quality of Thermoplastic Composite Laminate. J. Compos. Sci. 2021;5(3):88.

[3] Schledjewski R. Thermoplastic tape placement process – in situ consolidation is reachable. Plastics, Rubber and Composites 2009;38(9-10):379–86.

[4] SUCH M, Ward C, Potter K. Aligned Discontinuous Fibre Composites: A Short History. JMC 2014;2(3).

[5] Yarlagadda S, Deitzel J, Heider D, Tierney J, Gillespie Jr. JW. Tailorable Universal Feedstock for Forming (TuFF): Overview and Performance. In: SAMPE 2019 - Charlotte, NC. Proceedings; 05202019; 2019.

[6] Ryu S-R, Lee D-J. Effects of fiber aspect ratio, fiber content, and bonding agent on tensile and tear properties of short-fiber reinforced rubber. KSME International Journal 2001;15(1):35–43.

[7] Stodieck O, Cooper JE, Weaver PM, Kealy P. Improved aeroelastic tailoring using tow-steered composites. Composite Structures 2013;106:703–15.

[8] Lopes CS, Gürdal Z, Camanho PP. Variable-stiffness composite panels: Buckling and first-ply failure improvements over straight-fibre laminates. Computers & Structures 2008;86(9):897–907.

[9] Smith B, Brooks T, Leader M, Chin TW, Kennedy G, Martins JR et al. Passive Aeroelastic Tailoring. Paris: Seuil; February/2020.

[10] Clancy G, Peeters D, Oliveri V, Jones D, O'Higgins RM, Weaver PM. A study of the influence of processing parameters on steering of carbon Fibre/PEEK tapes using laser-assisted tape placement. Composites Part B: Engineering 2019;163:243–51.

[11] Lozano GG, Tiwari A, Turner C, Astwood S. A review on design for manufacture of variable stiffness composite laminates. Proceedings of the

Institution of Mechanical Engineers, Part B: Journal of Engineering Manufacture 2016;230(6):981–92.

[12] Blom A. Structural performance of fiber-placed, variable-stiffness composite conical and cylindrical shells. [S.l.: s.n.]; 2010.

[13] Lamontia M, Funck S, Gruber M, Cope R, Waibel B, Gopez N. Manufacturing Flat and Cylindrical Laminates and Build up Structure using Automated Thermoplastic Tape Laying, Fiber Placement and Filament Winding. SAMPE 2002.

[14] Nagendra S, Kodiyalam S, Davis J, Parthasarathy V. Optimization of tow fiber paths for composite design. In: 36th Structures, Structural Dynamics and Materials Conference. Reston, Virigina: American Institute of Aeronautics and Astronautics; 04101995.

[15] Beakou A, Cano M, Le Cam J-B, Verney V. Modelling slit tape buckling during automated prepreg manufacturing: A local approach. Composite Structures 2011;93(10):2628–35.

[16] Bakhshi N, Hojjati M. An experimental and simulative study on the defects appeared during tow steering in automated fiber placement. Composites Part A: Applied Science and Manufacturing 2018;113:122–31.

[17] Rajasekaran A, Shadmehri F. Steering of carbon fiber/PEEK tapes using Hot Gas Torch-assisted automated fiber placement. Journal of Thermoplastic Composite Materials 2022.

[18] Smith RP, Qureshi Z, Scaife RJ, El-Dessouky HM. Limitations of processing carbon fibre reinforced plastic/polymer material using automated fibre placement technology. Journal of Reinforced Plastics and Composites 2016;35(21):1527–42.

[19] Zhao C, Xiao J, Huang W, Huang X, Gu S. Layup quality evaluation of fiber trajectory based on prepreg tow deformability for automated fiber placement. Journal of Reinforced Plastics and Composites 2016;35(21):1576–85.

[20] Kim BC, Weaver PM, Potter K. Manufacturing characteristics of the continuous tow shearing method for manufacturing of variable angle tow

composites. Composites Part A: Applied Science and Manufacturing 2014;61:141–51.

[21] Larberg YR, Akermo M. In-Plane Properties of Cross-Plied Unidirectional Prepreg. In: ICCM16, editor. Proceedings of the 16th international conference on composite materials; 2007.

[22] Kim BC, Potter K, Weaver PM. Continuous tow shearing for manufacturing variable angle tow composites. Composites Part A: Applied Science and Manufacturing 2012;43(8):1347–56.

[23] Fidlow H, Cender TA, Simacek P, Yarlagadda S, Advani SG. Extensional viscosity of thermoplastic TuFF composites in stretch forming process. In: SAMPE 2022 - Charlotte, NC. Proceedings; 2022.

[24] Cender TA, Fidlow H, Yarlagadda S, Heider D, Simacek P, Advani SG et al. Forming limits of TuFF Composites in stretch forming processes. In: SAMPE 2022 - Charlotte, NC. Proceedings; 2022.

[25] Fuessel L, Cender TA, Austermann V, Gillespie Jr. JW, Heider D. Tow Steering of stretchable TuFF thermoplastic tape with laser tape placement. In: SAMPE 2022 - Charlotte, NC. Proceedings; 2022.

[26] Rajan S, Sutton MA, Wehbe R, Tatting B, Gurdal Z, Kidane A. Measured Surface Deformation and Strains in Thin Thermoplastic Prepreg Tapes Steered along Curved Paths without Adhesion Using StereoDIC. Exp Mech 2019;59(4):531–47.

[27] Rajan S, Sutton MA, Wehbe R, Tatting B, Gürdal Z, Kidane A et al. Experimental investigation of prepreg slit tape wrinkling during automated fiber placement process using StereoDIC. Composites Part B: Engineering 2019;160:546–57.

[28] Sloan J. AFP tow steering comes of age: Part 1: Current state. [March 27, 2023]; Available from: https://www.compositesworld.com/articles/afp-tow-steering-comes-of-age-part-1-current-state.

[29] Denkena B, Schmidt C, Völtzer K, Hocke T. Thermographic online monitoring system for Automated Fiber Placement processes. Composites Part B: Engineering 2016;97:239–43.

[30] Yadav N, Oswald-Tranta B, Schledjewski R, Wachtarczyk K. Ply-by-ply inline thermography inspection for thermoplastic automated tape layup. Advanced Manufacturing: Polymer & Composites Science 2021;7(3-4):49–59.

[31] Schmidt C, Denkena B, Hocke T, Völtzer K. Influence of AFP Process Parameters on the Temperature Distribution Used for Thermal in-process Monitoring. Procedia CIRP 2017;66:68–73.

[32] Croft K, Lessard L, Pasini D, Hojjati M, Chen J, Yousefpour A. Experimental study of the effect of automated fiber placement induced defects on performance of composite laminates. Composites Part A: Applied Science and Manufacturing 2011;42(5):484–91.

[33] Woigk W, Hallett SR, Jones MI, Kuhtz M, Hornig A, Gude M. Experimental investigation of the effect of defects in Automated Fibre Placement produced composite laminates. Composite Structures 2018;201:1004–17.

[34] Lukaszewicz DH-J, Ward C, Potter KD. The engineering aspects of automated prepreg layup: History, present and future. Composites Part B: Engineering 2012;43(3):997–1009.

[35] Schmidt C, Hocke T, Denkena B. Artificial intelligence for non-destructive testing of CFRP prepreg materials. Prod. Eng. Res. Devel. 2019;13(5):617–26.

[36] Samuel AL. Some Studies in Machine Learning Using the Game of Checkers. IBM J. Res. & Dev. 1959;3(3):210–29.

[37] Sacco C, Baz Radwan A, Anderson A, Harik R, Gregory E. Machine learning in composites manufacturing: A case study of Automated Fiber Placement inspection. Composite Structures 2020;250:112514.

[38] Wanigasekara C, Oromiehie E, Swain A, Prusty BG, Nguang SK. Machine Learning Based Predictive Model for AFP-Based Unidirectional Composite Laminates. IEEE Trans. Ind. Inf. 2020;16(4):2315–24.

[39] Wanigasekara C, Oromiehie E, Swain A, Prusty BG, Nguang SK. Machine learning-based inverse predictive model for AFP based thermoplastic composites. Journal of Industrial Information Integration 2021;22:1–8.

[40] Marani R, Palumbo D, Galietti U, Stella E, D'Orazio T. Automatic detection of subsurface defects in composite materials using thermography and

unsupervised machine learning. In: 2016 IEEE 8th International Conference on Intelligent Systems (IS): IEEE; 2016, p. 516–521.

[41] O'Shea K, Nash R. An Introduction to Convolutional Neural Networks; 2015.

[42] Albawi S, Mohammed TA, Al-Zawi S. Understanding of a convolutional neural network. In: 2017 International Conference on Engineering and Technology (ICET): IEEE; 2017 - 2017, p. 1–6.

[43] Gu J, Wang Z, Kuen J, Ma L, Shahroudy A, Shuai B et al. Recent advances in convolutional neural networks. Pattern Recognition 2018;77:354–77.

[44] Aghdam HH, Heravi EJ. Guide to convolutional neural networks: A practical application to traffic-sign detection and classification / Hamed Habibi Aghdam, Elnaz Jahani Heravi. Cham, Switzerland: Springer; 2017.

[45] Goodfellow I, Bengio Y, Courville A. Deep learning. Cambridge, Massachusetts: The MIT Press; 2016.